

ГОДИШНИК НА СОФИЙСКИЯ УНИВЕРСИТЕТ „СВ. КЛИМЕНТ ОХРИДСКИ“
ФИЗИЧЕСКИ ФАКУЛТЕТ, ЮБИЛЕЙНО ИЗДАНИЕ
130 ГОДИНИ СОФИЙСКИ УНИВЕРСИТЕТ
и 55 ГОДИНИ ФИЗИЧЕСКИ ФАКУЛТЕТ
„Нови научни постижения и направления във Физически факултет“

ANNUAL OF SOFIA UNIVERSITY “ST. KLIMENT OHRIDSKI”
FACULTY OF PHYSICS, JUBILEE EDITION
130th ANNIVERSARY OF SOFIA UNIVERSITY
and 55th ANNIVERSARY OF FACULTY OF PHYSICS
“New scientific achievements and directions in the Faculty of Physics”

MANIPULATION OF THE TOPOLOGICAL CHARGES OF OPTICAL VORTICES: RECENT RESULTS

LYUBOMIR STOYANOV¹, GEORGI MALESHKOV¹, MAYA ZHEKOVA¹, SUZANA
TOPUZOSKI², IVAN STEFANOV¹, GERHARD PAULUS^{3,4}, ALEXANDER DREISCHUH¹

¹*Department of Quantum Electronics, Faculty of Physics, Sofia University*

²*Faculty of Natural Sciences and Mathematics, Institute of Physics,
University “Ss. Cyril and Methodius”, Skopje-1000, Republic of Macedonia*

³*Institute of Optics and Quantum Electronics, Friedrich Schiller University
Max-Wien-Platz 1, D-07743 Jena, Germany*

⁴*Helmholtz Institute Jena, Helmholtzweg 4, D-07743 Jena, Germany*

*Любомир Стоянов, Георги Малешков, Мая Жекова, Сузана Топузоски, Иван Стефанов,
Герхард Паулус, Александър Драйшу.* МАНИПУЛИРАНЕ НА ТОПОЛОГИЧНИТЕ ЗАРЯДИ НА
ОПТИЧНИ ВИХРИ: СКОРОШНИ РЕЗУЛТАТИ

В тази работа представяме оптичните вихри (ОВ) и техните основни характеристики. Показано е, че една от тях, топологичният заряд (ТЗ), може да се манипулира контролирано, водейки до промяна на формата на снопа в далечната зона. ТЗ определя и основните взаимодействия между ОВ. Генерирани са големи решетки, съставени от стотици ОВ с алтернативни ТЗ. Показано е, че контролираното манипулиране на ТЗ на вихрите в такива решетки води до драматична промяна на формата на снопа. Проста алгебра с ТЗ е установена и в нелинейните режими на четиривънново смесване, и на генериране на високи хармонични.

For contact: Alexander Dreischuh, Faculty of Physics, Sofia University “St. Kliment Ohridski”,
5 J. Bourchier Blvd., BG-1164 Sofia, Bulgaria, Phone: +359 2 8161 611 and + 359 888 252 829,
E-mail: ald@phys.uni-sofia.bg.

In this paper we introduce the optical vortices (OVs) and their main characteristics. It is shown that one of them, the topological charge (TC), can be controllably manipulated leading to far-field beam reshaping. The TCs rule also the fundamental interactions between OVs. OV lattices composed from hundreds of OVs with alternating TCs are generated. The controllable manipulation of the TCs of the vortices in such lattices is shown leading to a dramatic beam reshaping. Simple vortex TC algebra is ascertained also in the nonlinear regimes of four-wave frequency mixing and high harmonic generation.

Keywords: singular optics, optical vortices, wave propagation, spatial light modulators
PACS numbers: 42.30.Kq, 42.40.Jv, 42.60.Jf, 42.65.Ky

1. INTRODUCTION

Optical vortices (OVs) are two-dimensional singular beams with spiral phase dislocations in their wavefronts [1]. OVs carry photon angular momentum, which can be transferred to matter and it is referred to as the topological charge (TC). The TC m is a positive or negative integer number corresponding to the total phase change $2\pi m$ over the azimuthal coordinate φ . It is known that a pair of singly and equally charged OVs placed on a bright background beam, rotate and repel each other [2, 3], whereas OVs of opposite TCs translate with respect to the background beam, attract each other and eventually annihilate. For the first time the possibility to stabilize ensembles of equally-charged OVs against rotation by a suitable choice of the topological charge of a “control OV” nested in the ensemble center is proved numerically in [4]. Specifically, if an OV with a TC opposite to the TCs of the rest of the OV ensemble is positioned in the center of the structure, the rotation of the entire ensemble is suspended. An extension of such vortex ensembles towards large stable regular OV lattices is also analyzed in [4] and studied for the first time experimentally in [5].

Vortices are ubiquitous in nature and have become a research topic in many areas of physics, ranging from fluid dynamics [6] to cold atoms [7]. OVs have found useful applications in optical manipulation of small particles [8], in optical imaging [9], as potential information carriers in data transmission [10], in interferometry [11], high-resolution microscopy and lithography [12], in spectroscopy [13, 14], just to mention a few areas.

2. BASIC INTERACTIONS OF OPTICAL VORTICES

Fig. 1 is visualizing the basic interaction scenarios between two OVs nested on a common bright background beam. In the upper left panel of fig. 1 the spiral phase profile of a singly charged OV is shown. The directions of the vectors in

the respective vector plot shown in the frame below clearly indicate its rotation on the background beam. The bottom left frame in the same figure is an experimentally obtained intensity distribution of such an OV. Since it does not change its position on the background beam, the dashed line crossing all experimental frames could be regarded as a reference for the rotation/translation of OV pairs of equal/opposite TCs. In the middle column of frames in fig. 1 we show that the two helical phase profiles of two equally charged OVs (upper frame) lead to an overall helicity of the phase (middle frame) and, as a consequence, to the rotation of the OV pair with respect to their “center of gravity” (bottom frame). In the case of OVs with opposite TCs equal to 1 and -1, there is a phase gradient along a line perpendicular to the line connecting the OV cores (right column, vector plot). Hence, the OV pair is translating on the background beam, which can be clearly seen in the experimental result (lower right frame in fig. 1).

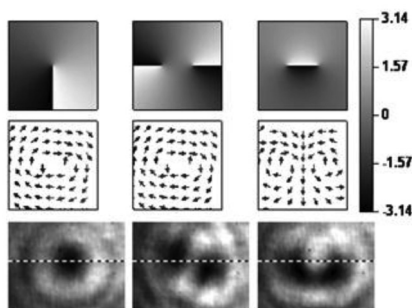


Fig. 1. Phase profiles (upper row) and vector plots (middle) of a single OV (left column), of two OVs with equal unit topological charges (middle column), and of two OVs with opposite unit topological charges (right column). Lower row – experimental data obtained at an initial OV-to-OV separation 57 pix. and at a distance of free space propagation of 32 cm

3. ARITHMETICS WITH THE TC OF A SINGLE OPTICAL VORTEX

The intensive research in the field of singular optics has shown that OV beams can be generated from incident chargeless optical beams by means of diffractive optical elements (DOEs) with embedded phase dislocations, such as spiral phase plate, helical axicon, and spiral zone plates [15] as well as with fork-shaped gratings [16–19] and spatial light modulators. Here we report results obtained by using the last two approaches. The underlying physics in manipulating the TCs of OVs is based on the results published in [20, 21]. The authors have shown theoretically that in the process of diffraction of Laguerre-Gaussian beam (with radial mode number equal to zero and with an arbitrary azimuthal mode number l), by a fork-shaped grating (with an integer forked dislocations p), in the

positive and negative m -th diffraction order, the diffracted beam carries topological charge s which is determined as an algebraic sum $s = 1 + mp$ or $s = 1 - mp$, respectively. Here we provide experimental evidences (fig. 2) for this rule (visualised in fig. 3) [22]: The final TC of the vortex is equal to the TC of the incident beam plus the diffraction order (with its sign) times the TC encoded in the binary grating. As a consequence from this transformation rule, OV TC can be erased in one case when the resultant TC equals to zero. As a result, in the focal plane of a lens (and in the far field) a well formed single bright peak is formed at the former position of the OV dark core. Some experimental data [22] are shown in figs. 4 and 5. In order to quantify how much these beams differ from Gaussian beams we used Gaussian fits to the respective beam cross-sections. The normalized root mean square deviation between each pair of curves was found to be between 0.034. The respective correlation coefficients varied between 0.95 and 0.98 thus indicating high-quality Gaussian beam shapes. The theoretical results [20, 21] for the algebraic transformation of the TCs of the OVs and for the vortex ring radii of the transformed beams vs. final TC are also found to be in an excellent agreement with the obtained experimental data.

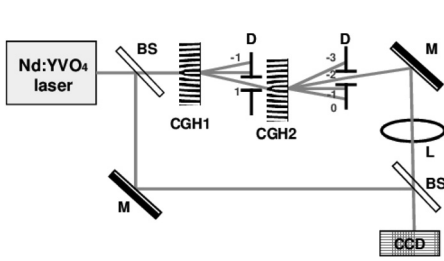


Fig. 2. Experimental setup: Nd:YVO₄ laser emitting at $\lambda = 532$ nm, BS – beam splitters. CGH1, CGH2 – binary computer-generated holograms, D – diaphragms, L – focusing lens ($f = 100$ cm), M – flat mirrors. CCD camera located at the beam waist

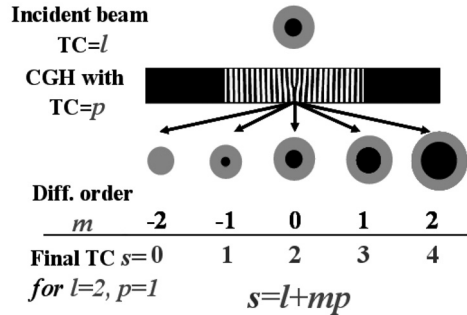


Fig. 3. Sketch of the transformation rule of the topological charge of the incident OV beam in the case of $l = 2$ and $p = 1$. See the text for details. The larger the dark spot, the higher the topological charge of the vortex

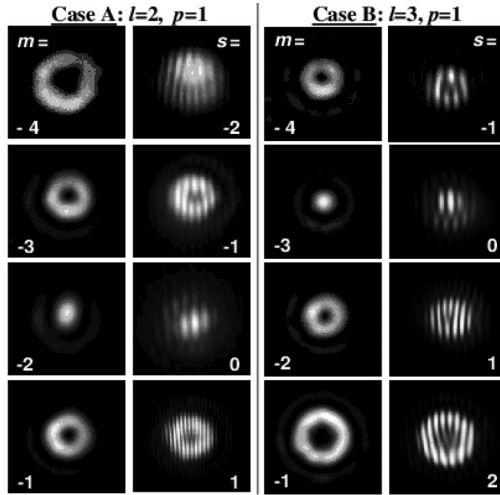


Fig. 4. Power density distributions and respective interferograms for identifying the resultant OV TCs (respective right columns) of the OV beams diffracted in different orders m of CGH2 encoded with an singly-charged OV ($p=1$) see figs. 2 and 3. Case A: $l = 2$ and Case B: $l = 3$

In the interferograms recorded with inclined plane waves the location and the magnitude of the OV TC can be easily recognized by the fork-like splitting of one interference line in q lines. In this case the TC is equal to $q-1$. The change in the direction of the splitting means an inversion of the sign of the TC. In fig. 4 we present some of the experimental data, from which the radial beam's cross-sections shown in fig. 5 are extracted. The data confirm that in the absence of a phase dislocation a well formed bright beam is recovered in the far field. Underlying preceding analysis and experiments devoted to the diffraction of a Gaussian beam by a four-sector binary grating are published in [23].

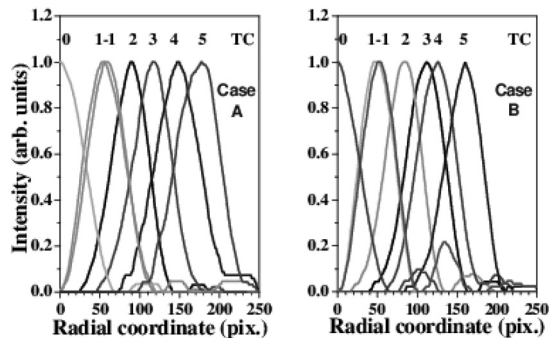


Fig. 5. Normalized radial cross-sections of the OV beams experimentally generated in Case A ($p = 1$ and $l = 2$; left graph) and in Case B ($p = 1$ and $l = 3$; right graph) in different diffraction orders and their TCs

Being encouraged by the results in [22, 23], and using the same experimental scheme (see fig. 2), we studied the diffraction of an OV beam from a computer-generated hologram (CGH) encoded with crossed one-dimensional phase dislocations with phase jumps of π between them [24]. The essential part of the used binary CGH is shown in the left frame in fig. 6. The amplitude profile of the beam diffracting in ± 1 -st diffraction order is X-modulated in azimuthal direction, with a central dark non-vortex core. Thereafter its diffraction from a CGH of an OV is studied. Both the theoretical model (fig. 6, middle frame) and the experimental data (fig. 6, right) confirm that this beam is transformed in the focal plane of a converging lens (artificial far field) into an array of five-vortex spot pattern [23].

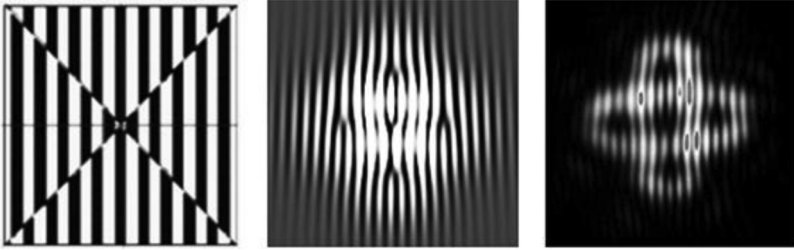


Fig. 6. Left: Binary computer-generated hologram (CGH) of a beam carrying crossed 1-D phase dislocations. Middle: Simulation of the derived theoretical result confirming that the diffraction of the X-shaped beam from a CGH of an OV results in a five-spot focal pattern. Right: Experimental result confirming the theoretical prediction

As seen in the interference patterns presented in fig. 6, the array consists of a central vortex (which value and sign of its TC depend on the diffraction order m ; in the presented case $|m| = 1$) and four “satellite” vortices situated in the apices of a rotated square which signs of the TCs are inverted and depend on the diffraction order m , in which they are nested. In a wide range of diffraction orders the data obtained experimentally confirmed the presence of the vortices (also the values and signs of their TCs) as predicted in [23].

4. MANIPULATION THE TOPOLOGICAL CHARGES OF LARGE OPTICAL VORTEX LATTICES

4.1. EXPERIMENTAL APPROACH

The experimental setup (fig. 7) involves a green pump beam from a frequency-doubled continuous-wave Nd:YVO₄ laser. It illuminates the reflective liquid-crystal spatial light modulator SLM1. This first modulator modulates the phase of the input Gaussian beam (and, as a consequence, also its amplitude/intensity) and redirects it to a second spatial light modulator SLM2 of the same type. The additionally modulated singular beam reflected from SLM2 is focused by a lens L ($f = 100$ cm) onto a CCD camera chip with a sensitive area of 7.1×5.4 mm (1600×1200 pix.). The distance between SLM2 and the lens is 95 cm. For diagnostic purposes, a reference beam is split off the laser beam before SLM1 by a beam splitter (BS1). The object and the reference beams are recombined by a second beam splitter (BS2) to interfere at the CCD camera chip. Power density distributions of the resulting optical beams and the respective interference patterns are recorded by the same CCD camera by blocking/unblocking the reference laser beam, while keeping the lens and camera positions unchanged. SLM1 and SLM2 are aligned parallel with a distance of 49 cm. The angle of incidence of the green laser beam is ~ 4 deg.

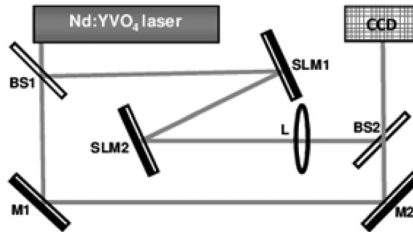


Fig. 7. Experimental setup. Nd:YVO₄ continuous-wave frequency-doubled laser emitting at a wavelength $\lambda = 532$ nm; BS, beam splitters; M, flat silver mirrors; SLM – reflective spatial light modulators (model Pluto, Holoeye Photonics); L, focusing lens ($f = 100$ cm); CCD, charge-coupled device camera

4.2. NUMERICAL MODEL

As seen from fig. 7, the propagation of the laser beam in the object arm of the interferometer is linear. Its evolution was numerically simulated by using the linear model equation for the slowly-varying optical beam envelope amplitude E

$$i\partial E / \partial(z/L_D) + (1/2)\Delta_T = 0. \quad (1)$$

Here Δ_T is the transverse part of the Laplace operator, $L_D = ka^2$ is the diffraction length of an individual OV, and k is the wave number in air. In a computational window spanning over 1024×1024 pix. the half width at the $1/e^2$ intensity level of the bright background Gaussian beam was 205 pix. Using SLM1, we created a single OV by pure phase modulation and recorded its profile just behind SLM1 at the position of SLM2. From such data we deduced that the SLM1-to-SLM2 distance corresponds to $1.5L_D$ and the SLM2-to-lens distance – to $3.0L_D$. The transmission phase function $T(x,y)$ of a thin lens with a focal length f

$$T(x,y) \cong \exp\{-ik(x^2 + y^2)/(2f)\} \quad (2)$$

was added to the phase distribution in the plane of the lens L (see fig. 7) and the beam evolution was numerically followed to the focal plane $41L_D$ behind the lens.

4.3. SQUARE OV LATTICES [25]

An ultimate numerical proof of the idea to manipulate the far field beam profiles by manipulating the TCs of large OV lattices would be, if a square OV array consisting of hundreds of OVs with alternating TCs is generated by SLM1 and all topological charges are set to zero (i.e. “erased”) by SLM2. Thus, a Gaussian beam should be recovered in the focus of the lens. This is clearly demonstrated in fig. 8 for vortex core-to-core separation 41 pix.

In the high-intensity region, the phase is almost flat as it should be when an unperturbed Gaussian beam is focused. We attributed the small deviation from perfect flatness to a numerical deviation of the modeled focal position from the “real” one due to the final step size.

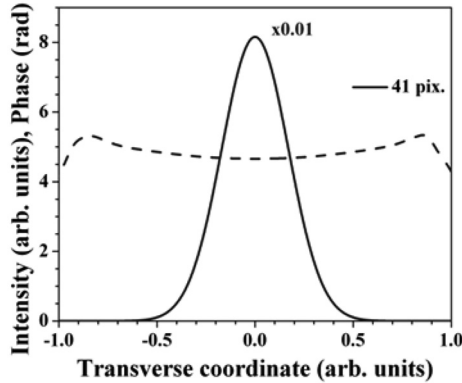


Fig. 8. Numerical data [25]. Far field intensity distributions (solid curve) of recovered Gaussian beam and its respective phase profiles (dashed curve) when all TCs of a large square OV array are erased by a second (oppositely charged) vortex array. The vortex array node spacing is 41 pix.

In fig. 9 we show [25] numerical simulations for the creation of a large square lattice of OV's with alternating TCs in the case of array node spacing equal to 41 pix. The intensity of the background beam illuminating SLM1 (see fig. 7) is shown in frame (a). The phase distribution sent to this modulator is visualized in frame (b) and the simulated resulting intensity distribution just in front of SLM2 is depicted in frame (c). When a phase distribution with inverted signs of the TCs is sent to SLM2, the entire array of singularities situated in squares is erased and the resultant phase profile is modulated but does not contain phase discontinuities anymore (frame (d)). As a result of the subsequent linear propagation before the focusing lens (see fig. 7), the dark beam contrast is gradually decreased (frame (e)). Due to the added phase profile in the plane of the lens (frame (f)) the beam is focused. The resultant intensity (frames (g, i)) and phase profiles (frames (h, j)) of the recovered Gaussian beams in the artificial far field and $6.5L_D$ behind it (i, j) are shown on the right hand side of fig. 9. In fig. 9h one can recognize that the phase front of the Gaussian beam in the focus of a lens is flat, as known from the theory. Behind the focus it becomes spherical, which is due to the additional $6.5L_D$ diffraction-influenced propagation behind the lens focus.

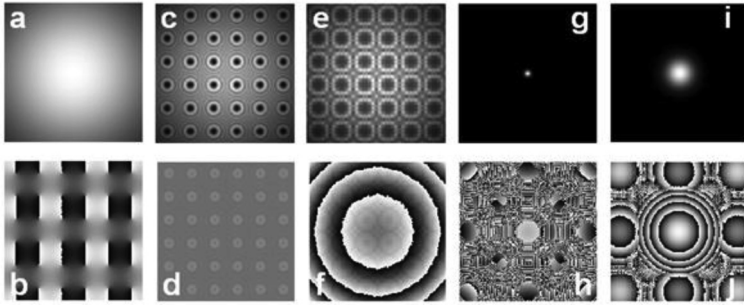


Fig. 9. Numerical simulations [25] for array node spacing 41 pix. Intensity of the background beam (a) illuminating SLM1, phase distribution sent to this modulator (b) and resulting intensity distribution just in front of SLM2 (c). After the inverted (in signs) TC phase distribution erases the whole array of square singularities, the phase profile is modulated but does not contain phase discontinuities (d) and, in front of the focusing lens, the dark beam contrast gradually decreases (e). The lens (phase profile just behind it shown in frame (f)) focuses the beam. Intensity (g, i) and phase profiles (h, j) of the recovered Gaussian beams in the artificial far field (g, h) and behind it (i, j)

Let us first describe the result of the far-field structure obtained when a large square optical vortex lattice is created only by one of the spatial phase modulators at a node spacing of 41 pix., while the second modulator is switched off acting as a mirror. In fig. 10 we show [25] numerical results (frames (a)-(f)) and compare them with experimentally observed ones ((g) and (h)). The calculated far-field intensity (frames (a) and (c)) and phase profiles (frames (b) and (d)) indicate that the observed four peaks situated in the apices of a rotated quadrature have flat phases

in the lens focus (frame (b)) and spherical phase profile behind it (frame (d)). The intensity distributions shown in frames (e) and (f) again correspond to far-field intensity profiles of large square optical vortex lattice but at a smaller node separation of 21 pix. Frames (a) and (e) provide a nice visualization of the well-known feature of the Fourier transformation performed by a thin lens, known as the Similarity theorem: “wide” functions in the time (space) domain correspond to “narrow” functions in the (spatial) frequency domain. This numerical result is in an excellent agreement with the experimental observations in this work and could serve as a control parameter for potential applications of such focused structures. In fig. 10g,h we show experimental results for OV’s separated by 41 pix. encoded on phase modulator SLM1. The comparison between frames (g) and (e) shows that in the experiment a weak central peak is present too, which is probably due to the discrete structure of the modulator array. The interference stripes in frame (h) are parallel across the four bright peaks indicating flat phases as suggested by the numerical simulation shown in frame (b).

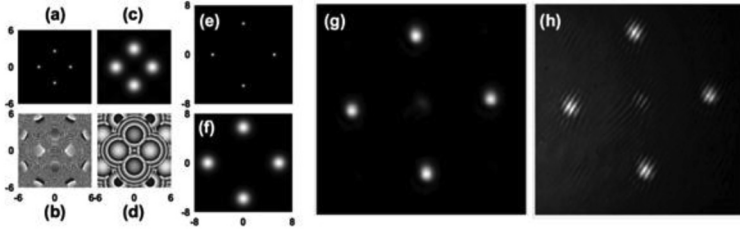


Fig. 10. Single square OV array – theory (a-f) vs. experiment (g, h). Far-field intensity (a, c, e-g) and phase (b, d) profiles of an square OV array, and respective interference pattern (h) for node spacing 41 pix.

In view of the above, it is natural to arrive at the idea to also use another known feature of the Fourier transformation, the Convolution theorem: The Fourier transform of the product of two functions is the convolution of their Fourier transforms. The experimental realization with two spatial phase modulators is simple: Let us assume that SLM1 and SLM2 add two different phase profiles to the initially flat phase of the incoming laser beam. The thin lens performs a two-dimensional Fourier transformation and in its focus we have to expect the convolution of the Fourier transformations of the phase and amplitude structures encoded by SLM1 and SLM2 separately. It is known that an OV nested symmetrically on its own background beam remains an OV in the focus of the lens. In view of the above it is not surprising that we observed the four peaks originating from the large OV array with an OV nested in each of the four bright peaks (see fig. 11a) when a single OV is encoded on SLM 2 and aligned such that it erases the TC of one OV from a large OV lattice produced by SLM1 in the artificial far-

field. Using the same base far-field structure originating from the large OV array encoded on SLM1, on SLM2 we encoded one-dimensional and quasi-two-dimensional spatial phase dislocations. The first line of intensity profiles in fig. 11 presents simulated far-field images resulting from combinations of the phase profiles of a large square array of OVs with alternating TCs with the phase profiles of an OV (fig. 11a), of an 1-D spatial phase dislocation (fig. 11b), and of a crossed 1-D (i.e. quasi-2-D) spatial phase dislocation (fig. 11c). Further, following the same ordering, we present the respective intensity (second row) and interference profiles of the experimentally observed far-field structures (last row). The presence of OVs is easily recognized in column ((a), last row) of fig. 11 by the four fork-like splittings of interference lines crossing the four bright peaks. The same upward direction of these splittings confirms that all 4 OVs have the same TCs. The interference patterns in fig. 11b and fig. 11c, last row, contain interference lines shifted along a line (a) or along two crossed lines (b) by a half of a period, thus indicating 1-D and quasi-2-D phase shifts of π and, hence, confirming the presence of spatial phase singularities.

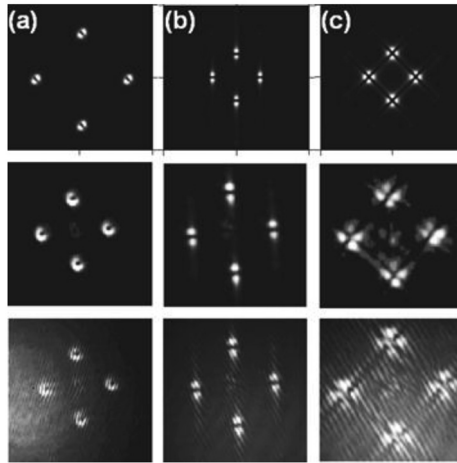


Fig. 11. Far field intensity profiles (first two rows) of square OV lattices structured by adding an OV with an opposite TC (a), one-dimensional dark beam (b), and crossed 1-D dark beams (c) [25]. First row – numerical results, last two rows – experimental data. See text for details

We confirmed that the results remain the same when the ordering of the phase distributions projected on the modulators is changed. Furthermore, they remain similar after changing the OV lattice node spacing. The TCs of the OVs placed in the four bright focal peaks in case (a) in fig. 11 can be reversed by reversing spatial phase profiles projected on the spatial light modulators.

In fig. 12 the upper row of frames (a)-(d) we shows results for a high-density square-shaped OV array with array node spacing $\Delta = 21$ pix. The phase profile of this array was encoded numerically on one of the SLMs. The resulting intensity (a) and phase profiles (b) just in front of the focusing lens L (see fig. 7) clearly show the result of some additional background beam modulation due to the simulated diffraction at a distance $z = 3L_{\text{diff}}$. One elementary cell of this OV lattice can be considered as composed by four OVs with identical unit TCs located in the apices of a square and one additional OV with an inverted sign nested in its center (see marked OVs in figs. 12e,f). After adding the respective phase of the focusing lens (fig. 12c) to the phase of the dense OV lattice (fig. 12b), the simulated four-spot far-field bright beam structure in the focal plane is shown in fig. 12d. In frames (e)-(h) of fig. 12 we keep the same ordering of the intensity and phase profiles, but this time for the case of square OV lattice of low density ($\Delta = 121$ pix.). Because the OVs in this case are well separated, the intensity modulation is in the form of grey rings surrounding each OV in frame (e), not as the modulation between the OV lattice nodes in frame (a) in fig. 12. Frames (c) and (g) are the same, since the action of the same focusing lens is modelled. The comparison between the far-field intensity profiles (d) and (h) is a clear demonstration of the validity of the already mentioned Similarity theorem.

Moreover, the vortices in frame (e) are obviously not centered with respect to the computational window, but the Fourier-transformed result (frame (h)) is. This is a nice visualization of the validity of the Shift theorem for the Fourier transformation. As the readers will see later, these numerical results are in an excellent agreement with the experimental observations. Therefore, the array node spacing $\Delta = 21$ pix. and $\Delta = 121$ pix.) of the square-shaped OV arrays are projected. This multi-spot focal array (ordered in a square composed of squares) is the typical one obtainable by mixing square OV arrays with different node spacings. The particular result corresponds to the cases separately illustrated in frames (a)-(d) and (e)-(h). The particular ordering on the phases on the SLMs was found to have negligible influence on the result. In the intensity profile denoted with the used magnification factor x1, one of the small-scale structures consisting of four peaks is marked. For better visibility the calculated phase profiles of these four beams are shown in the lower right frame with a magnification factor of x2.5. The encircled phase of two of the bright beams is obviously flat. Since black and white denote phases 0 and 2π , in the other two encircled phase areas phase singularities are absent too.

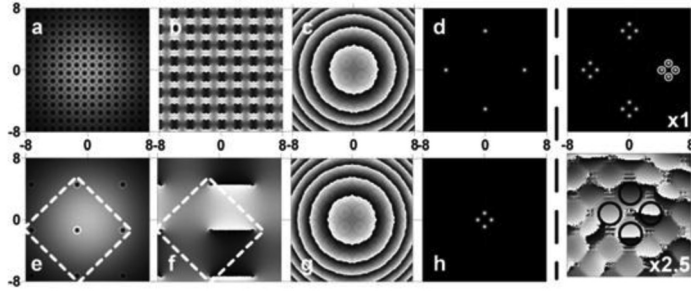


Fig. 12. Numerical results. High-density ($\Delta = 21$ pix.) square-shaped OV array (a) and its phase profile (b) at a distance $z = 3L_{\text{diff}}$ where the focusing lens ($f = 100$ cm corresponding to $z = 41L_{\text{diff}}$) is located. The resulting focal array is shown in frame (d). The respective numerical results for a low-density ($\Delta = 121$ pix.) OV array are shown in frames (e)-(h). Right: Multi-spot focal array simulated by creating the high-density OV array at the input plane of SLM1 ($z = 0$) and the low-density OV array by SLM2 at $z = 1.5L_{\text{diff}}$. The scaling factor x1 in the intensity distribution is marked to denote that the respective phase profile is magnified by a factor of 2.5 for better visibility. Circles – locations of the four peaks composing one element of the small-scale structure of the focal array

In fig. 13 we present experimental results which are in excellent agreement with the numerical ones. The close inspection of the interference pattern (frame (b)) shows parallel interference lines across the bright beams, which indicate that their phases are flat, as it should be in a focus of a lens. Nevertheless, we applied the four-frame technique for interferogram analysis [26, 27] in order to obtain quantitative information for the (horizontal) phase profiles of the beams in the sub-array marked in frame (b) in fig. 13. The respective data shown in the graph confirm that, with a reasonable accuracy, the reconstructed phases of the sub-beams are flat.

Fig. 14 summarizes the experimental data for the typical multi-spot focal bright beam arrays obtained when both SLMs are programmed with different square-to-square vortex array node distances. The array node spacings used in calculating the used phase profiles are marked in the same figure. As mentioned, the particular ordering of the phases on the SLMs has minor influence on the small-scale and on the large-scale structure of the multi-spot focal arrays. The *large-scale* structure is coming from the OV lattice with the smaller array node spacing, whereas the *small-scale* structure of the observed pattern results from the OV lattice with larger array node spacing. Weak influence on the noise due to the OV diffraction between the SLMs can be estimated only. The lower frames show the expected result when all OVs of the OV array are erased: Independent on the particular node spacing, a well formed single Gaussian bright peak is recovered in the focal plane (and in the artificial far field). The results show once again that the ratio between the OV lattice node spacings can be used as a control parameter for forming the desired multi-spot focal array. The data presented in fig. 14 are clear manifestation of both the Similarity and the Convolution theorems for the Fourier transformation.

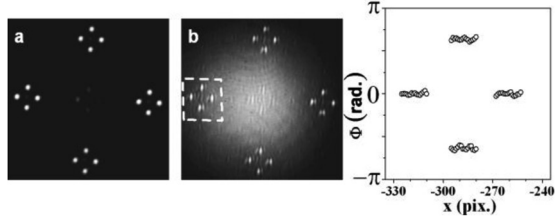


Fig. 13. Experimental results. Power density distribution of the observed multi-spot focal array (a) by programming SLM1 with the phase of the OV lattice with $\Delta = 121$ pix. and SLM2 – with this corresponding to $\Delta = 21$ pix. Frame (b) – the respective interferogram. The horizontal phase profiles of the four marked peaks in frame (b) are reconstructed in the graph to the right

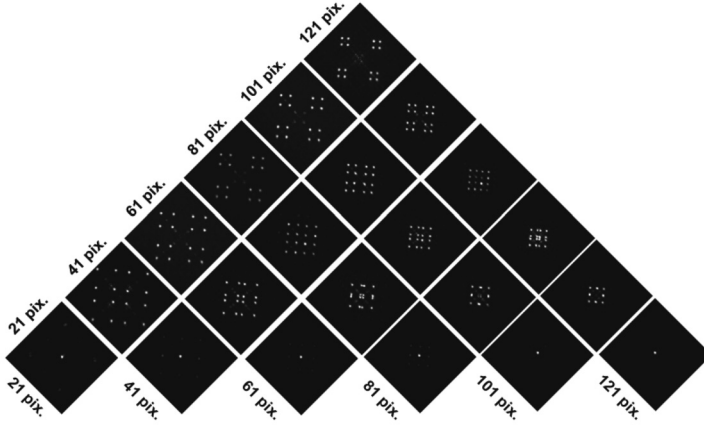


Fig. 14. Experimental results. Different focal arrays of bright beams observed by mixing two OV lattices of different square-to-square node spacings. The data show that the disposition of the peaks and their relative intensities remain the same when the ordering of the phase distributions on the SLMs is inverted. See the text for details

In fig. 15 we show experimentally that the generated multi-spot focal arrays of bright beams can be additionally structured by nesting an OV in each of these peaks. We prefer to demonstrate in details only this possibility, although 1-D and quasi-2-D dark beams can be formed in each of the peaks as done, in another configuration, in [25] (see fig. 11). Each experimentally recorded intensity distribution is accompanied by its respective interference pattern. In these patterns the location of the additionally nested OVs and their TCs can be easily recognized by the typical (for an interference with a plane wave) fork-like splitting of one interference line. Characteristic for the presented results is that in one interference pattern all fork-like splitting are oriented in the same direction, i.e. all inscribed OVs have the same sign of the TCs. The pairs of frames (a) and (b) indicate that embedding of a singular beam in each bright component of the multi-spot structure is possible in all cases shown in fig. 14. The pairs of frames (c) and (d) provide

evidence for an additional possibility for creating other multi-spot focal arrays when OV lattices of the same node spacing are used but, this time, at a controllable non-zero spatial offset. Additional structuring of the resulting focal peaks with singular beams is applicable in this case too.

4.4. HEXAGONAL OV LATTICES [28]

In this subsection we demonstrate numerically and experimentally the formation of another eight different basic structures consisting of bright beams with flat phase fronts in the focus of a lens (i.e. in the artificial far field) [28]. In all considered cases the used input structure is a large, stable, hexagon-shaped optical vortex (OV) array composed of vortices with alternating topological charges. Following the style of presentation used for figs. 9 and 12, in fig.16 we show numerical simulations for the creation of a large hexagonal lattice of OVs with alternating TCs in the case of array node spacing equal to 41 pix.

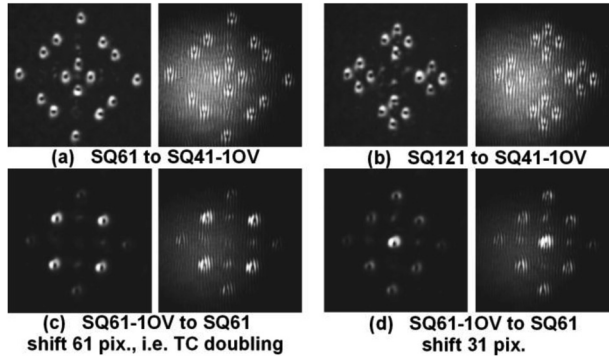


Fig. 15. Experimental results. Additional structuring of multi-spot focal arrays by erasing the TC of one OV in one of the OV arrays. Frames (a) and (b) show examples for an additional focal array structuring at different node spacings of the mixed OV lattices by imposing an additional OV. Pair of frames (c) and (d) – focal beam structuring when OV lattices of the same node spacing are shifted by one (c) and by a half of the square lattice period (d)

The intensity profile of the background beam illuminating SLM1 (see fig. 7) is shown in frame (a). The phase distribution sent to this modulator is visualized in frame (b) and the simulated resulting intensity distribution just in front of SLM2 is depicted in frame (c). When a phase distribution with inverted signs of the TCs is sent to SLM2 in an on-site alignment, the entire array of singularities situated in hexagons is erased and the resultant phase profile is modulated but does not contain phase discontinuities anymore (frame (d)). As a result of the subsequent linear propagation before the focusing lens (see fig. 7), the dark beam contrast is gradually decreased (frame (e)). Due to the added phase profile in the plane of the lens (frame (f)) the beam is focused. The resultant intensity (frames (g, i)) and

phase profiles (frames (h, j)) of the recovered Gaussian beams in the artificial far field (g, h) and $6.5L_D$ behind it (i, j) are shown on the right side of fig. 16. In fig. 16h one can recognize that the phase front of the Gaussian beam, in the focus of a lens, is flat, as known from theory. Behind the focus it becomes spherical, which is due to the additional diffraction-influenced propagation behind the lens focus. Some 6% of the total computational area is shown in each frame in fig. 16 spanning over (-6,6) arbitrary units.

In fig. 17 we show numerical results (frames (a)-(d)) and compare them with experimentally observed ones (frames (e)-(h)). The calculated far-field intensity (frames (a) and (c)) and phase profiles (frames (b) and (d)) indicate that the observed three dominating peaks situated in the apices of a triangle have flat phases in the lens focus (frame (b)). This triangle-like structure of bright peaks is built in (inscribed) in a rotated triangle-like structure of gradually less intense beams. The far-field phase profiles of these three additional beams appeared again to be flat. The intensity distributions shown in frames (c) and (d) again correspond to far-field intensity and phase profiles of large hexagonal optical vortex lattice but at a smaller node separation of 21 pix. Frames (a) and (c) provide a nice visualization of the well-known and already mentioned Similarity theorem.

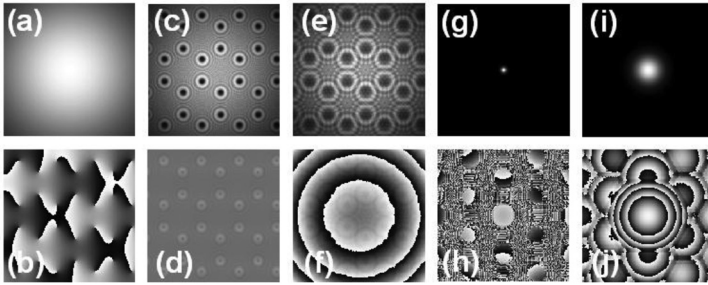


Fig. 16. Numerical simulations for hexagonal OV lattice with array node spacing 41 pix. [28]. Intensity of the background beam (a) illuminating SLM1, phase distribution sent to this modulator (b) and resulting intensity distribution just in front of SLM2 (c). After the whole array of hexagonal-ordered singularities is erased, the phase profile is modulated but does not contain phase discontinuities (d) and, in front of the focusing lens, the dark beam contrast gradually decreases (e). The lens (phase profile just behind it shown in frame (f)) focuses the beam. Intensity (g, i) and phase profiles (h, j) of the recovered Gaussian beams in the artificial far field (g, h) and $6.5L_D$ behind it (i, j)

This numerical result is in an excellent agreement with the experimental observations in [28] and could serve as a control parameter for potential applications of such focused structures. In fig. 17e,f we show experimental results obtained with OVs separated by 41 pix. encoded on phase modulator SLM1. Note that the orientation of the images in frames (e) and (f) differs by 180 deg. because of the inversion of the signs of all TCs of the OVs of the hexagonal lattice. The comparison between frames (c) and (e) shows that not only the peak dispositions, but also the relative intensities

of the observed six peaks are qualitatively similar. The interference stripes in frames (g) and (h) are parallel across all bright peaks indicating flat phases as suggested by the numerical simulation shown in frames (b) and (d).

We were able to additionally host an OV, an 1-D or a quasi-2-D singular beam in each of these three dominating peaks by deleting one OV of the array or by adding the singular phase profiles characteristic for the aforementioned 1-D and quasi-2-D singular beams. Since the results are similar to these shown in fig. 11 except the disposition of the peaks in the apices of a triangle, we refrain from showing them here. Instead of this, we prefer to show other possible approaches for a controllable shaping of bright structures in the focal plane of a lens. The far-field structures shown in fig. 18a-f are obtained by sending two identical phase distributions of large hexagonal OV lattices to both SLM1 and SLM2. Off-site alignment here means that the phase distribution at one of the modulators is shifted later on vertically (frames (a)-(c)) or horizontally (frames(d)-(f)) with respect to the phase distribution on the other modulator at a half of the lattice period. One can clearly see in the simulation (frame (a)) that among the 6 bright peaks of the hexagon two are slightly dominating. This is confirmed also by the measurement shown in frame (b).

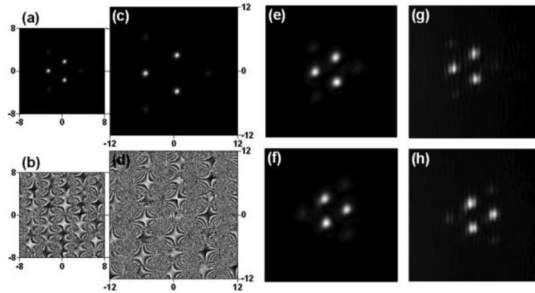


Fig. 17. Single hexagonal OV array – theory (a-d) vs. experiment (e-h) [28]. Far-field intensity (a, c, e, f) and phase (b, d) profiles of a hexagonal OV array, and respective interference patterns (g, h) for node spacing 41 pix. (a, b) and 21 pix. (c, d). In the experiment (frames (e-h)) the node spacing is 41 pix. See the text for details

In the second row of frames in fig. 18 we show calculated (d) and experimentally obtained (e) far-field intensity distribution consisting, again, of 6 dominating bright peaks located in the apices of a hexagon. They are obtained by a horizontal off-set of the described type by a half of the lattice period. The formed peaks here are of nearly equal intensity. The parallel interference stripes in the respective interference pattern (c) and (f) clearly indicate that the observed bright peaks in both cases have flat phase fronts.

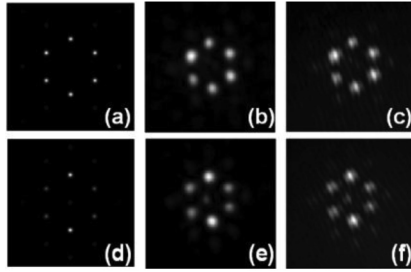


Fig. 18. Far field intensity profiles (a, b, d, e) modeled numerically (a, d) and recorded experimentally (b, e) when the OV lattices are displaced at a half of the lattice period vertically (a-c) or horizontally (d-f). Frames (c) and (f) show the respective interference patterns. Node spacing 41 pix in the simulations and 151pix. in the experiment

The relatively small differences in the intensities of the peaks in frames (a) and (d) (and frames (b) and (e), respectively) are probably due to additional small phase shifts between the lattices projected on SLM1 and SLM2, however we will refrain from speculating on this. Spectacular far-field beam reshaping resulting from the interaction between the two hexagonal OV lattices when all TCs of all OVs are doubled is shown in fig. 19 [28]. Columns (a) and (b) contain numerical results obtained for lattice node spacing 41 pix. and 21 pix. Column (c) shows the respective experimental result. The reshaped array of bright beams can be described as an equilateral triangle. Each cathetus of this triangle is marked with 5 bright peaks. In the centre of the large triangle an additional small equilateral triangle marked with 3 bright peaks is inscribed. This description, even somewhat cumbersome, adequately describes the structure consisting of 15 peaks. Regarding the relative beam intensities of the peaks within this structure, the situation predicted numerically (fig. 19a,b) and observed experimentally (fig. 19c) is even more interesting. Within the “solid” equilateral triangle marked with 15 bright peaks an inverted equilateral triangle marked with 6 peaks seems to be inscribed.

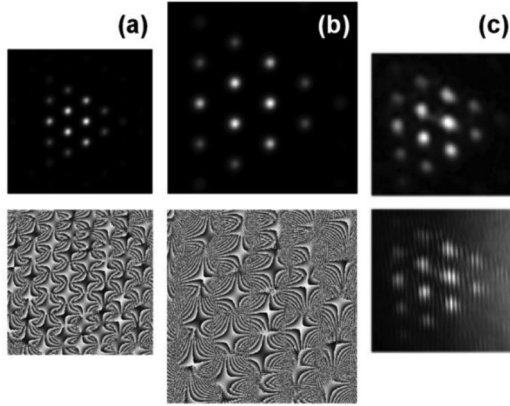


Fig. 19. Far field intensity profiles (a-c) modelled numerically (a, b) at lattice node spacing 41 pix. (a) and 21 pix. (b) and the respective phase profiles (lower frames). In column (c) the experimentally recorded intensity distribution (up) and the respective interference pattern are shown (down) for node spacing 151pix. [28]

4.5. MIXED SQUARE-SHAPED AND HEXAGONAL OV LATTICES

In this subsection we will start directly describing some experimental results which, nevertheless, are found to be in an excellent agreement with the numerical simulations. In frame (a) of fig. 20 the OVs constituting one elementary cell of the hexagonal lattice are encircled in order to clearly show the large ratio between the node spacings of the square and hexagonal lattices (a, b) and the broadening of each one of the OVs of the square lattices propagating from SLM1 to SLM2 as compared to the width of the newly-born OVs just after SLM2. The diffraction they experience until reaching the focusing lens is clearly seen in frame (b). Experimentally recorded far-field intensity distribution in fig. 20 too. As seen in frame (e), the experimental data perfectly match the numerical ones (frame (c)).

Moreover it is confirmed again, (numerically and experimentally) that the small-scale triangular structures of sub-beams can be rotated by 180° by inverting the signs of all TCs of the OVs constituting the hexagonal lattice or by changing the order of the creation of the individual lattices on the SLMs. The detailed inspection of the numerically obtained phase profile given in frame (d) shows that all bright sub-peaks have flat phases. This is in agreement with the observed parallel interference stripes in the experiment (frame (f)) when the beam in the reference arm of the interferometer (fig. 7) is slightly inclined with respect to the beam in its object arm.

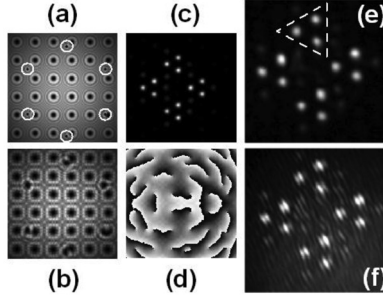


Fig. 20. Numerical simulations (a-d) and experimental results (e, f). Square-shaped OV array with a lattice constant 41 pix. is encoded on SLM1. Hexagonal OV lattice with lattice node spacing of 101 pix. is encoded on SLM2. Intensity distribution just behind SLM2 (a) and in front of the focusing lens L (b). Calculated far-field intensity distribution (c) and its respective phase profile (d). Experimentally recorded intensity distribution (e) and interference pattern (f) of the mixed lattices for the same ratio between their lattice constants. Dashed triangle – small-scale structure of the square-shaped large-scale beam structure

In fig. 21 we show different experimentally recorded far-field bright beam intensity distributions obtained by varying the node spacing Δ_{sq} of the square-shaped (row (a)) or Δ_{hex} of the hexagonal OV lattice (row (b)). These data are demonstrating the change in the symmetry and in the size of the far-field beam structures by changing the vortex-to-vortex node spacing of one of the lattices (frame (e)) and interference patterns (frame (f)) of such mixed lattices are shown, keeping the respective spacing for the other lattice unchanged. In case (a), the hexagonal lattice node spacing is $\Delta_{hex} = 41$ pix. One can see again that for $\Delta_{sq} = 21$ pix. (row (a), left frame) the far-field beam profile has the *small-scale structure* resembling an equilateral triangle with three dominating peaks situated in its apices. In other words, the *small-scale* structure is the one of the hexagonal OV lattice, which has a two-fold *larger* node spacing, i.e. $\Delta_{hex} = 41$ pix. The *large-scale* focal structure resembles a rhomb with the aforementioned triangular small-scale structures in its apices. In other words, the *large-scale* structure is the one of the square OV lattice with the *smaller* node spacing $\Delta_{sq} = 21$ pix. In the other limiting case shown in the most right frame of fig. 21a, $\Delta_{hex} = 41$ pix. is kept unchanged and Δ_{sq} is increased from 21 pix. to 151 pix., whereas the *large-scale* structure is this of the hexagonal lattice with the *smaller* $\Delta_{hex} = 41$ pix. The results in fig. 21 clearly indicate that $\Delta = \Delta_{sq} / \Delta_{hex}$ could serve as a control parameter for generating the desired focused structure.

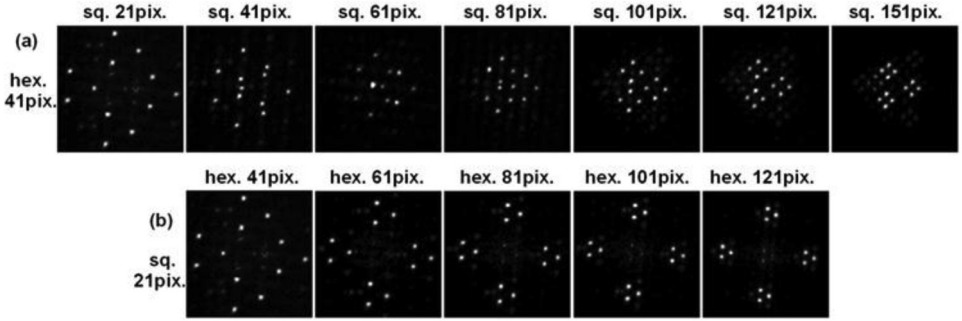


Fig. 21. Experimentally-recorded far-field beam reshaping by varying the node spacing of the square-shaped (a) or of the hexagonal OV lattice (b). In case (a) the hexagonal lattice node spacing is $\Delta_{\text{hex}} = 41$ pix. and $\Delta = \Delta_{\text{sq}}/\Delta_{\text{hex}}$ varies between 0.5 and 3.7. In case (b) $\Delta_{\text{sq}} = 21$ pix. and Δ varies between 0.5 and 0.17. See the text for details

5. TRANSFORMATION OF THE TCs IN NONLINEAR PROCESSES

We will very briefly describe our results on the transformation of the TCs of OVs in the second- and third-order perturbative nonlinear parametric processes of second harmonic generation (SHG) and four-wave frequency mixing (FWFM). In the process of SHG the TCs of the vortices become doubled [29]. Our analyses and experiments devoted to the diagnostics of pulse front tilts of femtosecond laser pulses [30] lead us to the idea to use an inverted field interferometer with/without a vortex lens on its input in order to switch between background-free and interferometric mode of measurement without any realignment of the autocorrelator. Experiments on this topic are under way. We have demonstrated [31] broadband cascaded mixing of vortex beams in a self-focusing Kerr medium. The nonlinear generation process, although not phase matched, was efficient enough to allow for observation of vortices over a bandwidth larger than 200nm. This [31] constituted the first measurement of topological charge for a multiply cascaded four-wave mixing process with vortex beams. Topological charge conservation for the nonlinear wave mixing process is found to be fulfilled, and decay of higher-order vortices into fundamental vortices has been observed [32] due to instability arising from the nonlinear self-focusing. In [33] we showed for the first time that optical vortices can be generated in the extreme ultraviolet (XUV) region using high-harmonic generation. The singularity impressed on the fundamental beam survives the highly nonlinear non-perturbative process. In a subsequent experiment [34] this was confirmed and it was proven that the TC of the XUV OV scales with the order of the high harmonic.

6. CONCLUSION

In this work we presented an overview of the possibilities for significant far-field beam reshaping by mixing square-shaped and hexagonal optical vortex lattices, as well as additional research toward the nonlinear behavior and transformation of an OV. Each of the singular lattices used here is composed of vortices with alternating TCs. The results may appear particularly interesting, as a new degree of freedom, for modifications in stimulated emission depletion (STED) microscopy, for extending the possibilities of generating singular higher-order vector fields [35], for controllable writing of parallel optically-induced waveguide structures e.g. in (photorefractive) nonlinear media (see, e.g., [36]) and may appear applicable for orbital angular momentum multiplexing of information [37] for data transfer using complex optical fields [38–40].

REFERENCES

- [1] Nye, J. F. and M. V. Berry. Proc. R. Soc. London Ser. A, 1974, **336**, 165.
- [2] Rozas, D., C. T. Law and G. A. Swartzlander, Jr. J. Opt. Soc. Am. B, 1997, **14**, 3054.
- [3] Rozas, D., Z. S. Sacks, and G. A. Swartzlander, Jr. Phys. Rev. Lett., 1997, **79**, 3399.
- [4] Neshev, D., A. Dreischuh, M. Assa, and S. Dinev. Optics Commun., 1998, **151**, 413.
- [5] Dreischuh, A., S. Chervenkov, D. Neshev, G. G. Paulus, and H. Walther. J. Opt. Soc. Am. B, 2002, **19**, 550.
- [6] Brandt, E. H., J. Vanacken, and V. V. Moshchalkov. Physica C, 2002, **369**, 1.
- [7] Matthews, M. R., B. P. Anderson, P. C. Haljan, D. S. Hall, C. E. Wieman, and E. A. Cornell. Phys. Rev. Lett., 1999, **83**, 2498.
- [8] Grier, D. G. Nature, 2003, **424**, 810.
- [9] Foo, G., D. M. Palacios, and G. A. Swartzlander. Opt. Lett., 2005, **30**, 3308.
- [10] Molina-Terriza, G., J. P. Torres, and L. Torner. Nature Physics, 2007, **3**, 305.
- [11] FÜRhapter, S., A. Jesacher, S. Bernet, and M. Ritsch-Marte. Opt. Lett., 2005, **30**, 1953.
- [12] Scott, T. F., B. A. Kowalski, A. C. Sullivan, C. N. Bowman, and R. R. McLeod. Science, 2009, **324**, 913.
- [13] Picón, A., A. Benseny, J. Mompart, J. R. Vázquez de Aldana, L. Plaja, G. F. Calvo, and L. Roso. New J. Phys., 2010, **12**, 083053.
- [14] Picón, A., J. Mompart, J. R. Vázquez de Aldana, L. Plaja, G. F. Calvo, and L. Roso., Optics Express, 2010, **18**, 3660.
- [15] Heckenberg, N. R., R. McDuff, C. P. Smith, and A. G. White. Opt. Lett., 1992, **17**, 221.
- [16] Vasara, A., J. Turunen, and A. T. Friberg. J. Opt. Soc. Am. A, 1989, **6**, 1748.
- [17] Bazhenov, V. Yu., M. V. Vasnetsov, and M. S. Soskin. Pisma Zh. Eksp. Teor. Fiz., 1990, **52**, 1037.
- [18] Heckenberg, N. R., R. McDuff, C. P. Smith, H. Rubinsztein-Dunlop, and M. J. Wegener. Opt. Quant. Electron., 1992, **24**, S951.
- [19] Terhalle, B., A. Langner, B. Päivänranta, V. A. Guzenko, C. David, and Y. Ekinci. Opt. Lett., 2011, **36**, 4143.
- [20] Topuzoski, S. and Lj. Janicijevic. J. Modern Optics, 2011, **58**, 138.
- [21] Topuzoski, S. and Lj. Janicijevic. Optics Commun., 2009, **282**, 3426.
- [22] Stoyanov, L., S. Topuzoski, I. Stefanov, L. Janicijevic, and A. Dreischuh. Optics Commun. 2015, **350**, 301.

- [23] Janicijevic, Lj., S. Topuzoski, L. Stoyanov, and A. Dreischuh. *Optics Commun.*, 2017, **389**, 203.
- [24] Topuzoski, S., Lj. Janicijevic, L. Stoyanov, I. Stefanov and A. Dreischuh. *Optics Commun.*, 2018, **428**, 206.
- [25] Stoyanov, L., G. Maleshkov, M. Zhekova, I. Stefanov, D. N. Neshev, G. G. Paulus, and A. Dreischuh. *J. Opt. Soc. Am. B*, 2018, **35**, 402.
- [26] Creath, C. In: IOP Publishing, Bristol, 1993, pp94.
- [27] Dreischuh, A., W. Fließner, I. Velchev, S. Dinev, and L. Windholz. *Appl. Phys. B*, 1996, **62**, 139.
- [28] Stoyanov, L., G. Maleshkov, M. Zhekova, I. Stefanov, G. G. Paulus and A. Dreischuh. *Journal of Optics*, 2018, **20**, 095601.
- [29] Basistiy, L. V., V. Yu. Bazhenov, M. S. Soskin, and M. V. Vasnetsov. *Opt. Commun.*, 1993, **103**, 422.
- [30] Dimitrov, N., L. Stoyanov, I. Stefanov, A. Dreischuh, P. Hansinger, and G. G. Paulus. *Optics Commun.*, 2016, **371**, 51.
- [31] Hansinger, P., G. Maleshkov, I. L. Garanovich, D. Skryabin, D. N. Neshev, A. Dreischuh, and G. G. Paulus. *Optics Express*, 2014, **22**, 11079.
- [32] Hansinger, P., G. Maleshkov, I. L. Garanovich, D. V. Skryabin, D. N. Neshev, A. Dreischuh, and G. G. Paulus. *J. Opt. Soc. Am. B*, 2016, **33**, 681.
- [33] Zürich, M., C. Kern, P. Hansinger, A. Dreischuh, and Ch. Spielmann. *Nature Physics*, 2012, **8**, 743.
- [34] Garipey, G., J. Leach, K. T. Kim, T.J. Hammond, E. Frumker, R. W. Boyd, and P.B. Corkum. *Phys. Rev. Lett.*, 2014, **113**, 153901.
- [35] Otte, E., K. Tekce, and C. Denz. *Optics Express*, 2017, **25**, 20194.
- [36] Stoyanov, L., N. Dimitrov, I. Stefanov, D. N. Neshev, and A. Dreischuh. *J. Opt. Soc. Am. B*, 2017, **34**, 801.
- [37] Li, S. and J. Wang. *Optics Express*, 2017, **25**, 21537.
- [38] Wang, J. *Photonics Research*, 2016, **4**, B14.
- [39] Wang, A., L. Zhu, L. Wang, J. Ai, S. Chen, and J. Wang. *Opt. Express*, 2018, **26**, 10038.
- [40] Du, J. and J. Wang. *Opt. Lett.*, 2017, **42**, 5054.